Thermoelectrics

Deutsche Ausgabe: DOI: 10.1002/ange.201505517
Internationale Ausgabe: DOI: 10.1002/anie.201505517

Thermoelectricity Generation and Electron–Magnon Scattering in a Natural Chalcopyrite Mineral from a Deep-Sea Hydrothermal Vent

Ran Ang, Atta Ullah Khan, Naohito Tsujii, Ken Takai, Ryuhei Nakamura,* and Takao Mori**

Abstract: *Current high-performance thermoelectric materials require elaborate doping and synthesis procedures, particularly in regard to the artificial structure, and the underlying thermoelectric mechanisms are still poorly understood. Here, we report that a natural chalcopyrite mineral, $Cu_{1+x}Fe_{1-x}S_2$, obtained from a deep-sea hydrothermal vent can directly generate thermoelectricity. The resistivity displayed an excellent semiconducting character, and a large thermoelectric power and high power factor were found in the low x region. Notably, electron–magnon scattering and a large effective mass was detected in this region, thus suggesting that the strong coupling of doped carriers and antiferromagnetic spins resulted in the natural enhancement of thermoelectric properties during mineralization reactions. The present findings demonstrate the feasibility of thermoelectric energy generation and electron/hole carrier modulation with natural materials that are abundant in the Earth's crust.*

Thermoelectric energy conversion technology has been utilized successfully as an electrical power supply for deep-space exploration, and has the strong potential for capturing and producing electricity from waste heat generated from various terrestrial applications. The past couple of decades have witnessed marked advances in the fundamental understanding of numerous thermoelectric materials and the underlying synthesis routes. For example, ternary chalcogenides serve as an ideal platform for investigating the intricate physical and chemical characteristics controlling the efficiencies of thermoelectric materials, and are also promising materials for potential applications in photovoltaics, luminescence, as well as thermoelectric and spintronic devices.[1–4] Ternary chalcopyrite-structured chalcogenides, such as $CuFeS_2$, have attracted particular attention owing to their unique optical, electrical, magnetic, and thermal properties.[5–19]

Studies on chalcopyrite ($CuFeS_2$) have primarily focused on its electronic states.[5,6,20–22] However, the molecular mechanisms controlling the electronic structure and thermoelectric properties of $CuFeS_2$, which may be influenced by the delocalization of Fe 3d electrons, charge-transfer-driven hybridization between the Fe 3d and S 3p orbitals, and the density of the conduction-band electron states, have not been resolved.[8,21,23] In addition, the fabrication of chalcopyrite requires complex synthesis procedures and relatively expensive constituent precursors, thereby potentially limiting the large-scale application of this thermoelectric material. Therefore, there is a need to identify new synthetic processes and/or inexpensive materials with efficient thermoelectric properties.

Here, we provide definitive evidence that thermoelectricity can be directly generated by a natural chalcopyrite mineral, $Cu_{1+x}Fe_{1-x}S_2$, obtained from a deep-sea hydrothermal vent. Measurement of the transport properties and theoretical analysis revealed that doped carriers have strong coupling with antiferromagnetic spins, which greatly enhance the thermoelectric power (S) and power factor, thus demonstrating the importance of electron–magnon scattering and large effective mass in thermoelectric performance. To our knowledge, this is the first report on the production of thermoelectricity by a naturally occurring chalcopyrite. The findings presented here may provide insight into approaches for producing low-cost thermoelectricity or electron/hole carriers from naturally abundant materials.

A series of natural chalcopyrite minerals, $Cu_{1+x}Fe_{1-x}S_2$ ($x = 0.17$, 0.08, and 0.02), were obtained from the Snow Chimney black smoker vent of the Mariner field in the southern Lau Basin.[24] Little variation in the mineral composition was observed in samples collected from different regions of intact natural sulfide chimneys, and minerals with the average composition were used as representative samples. The subsamples with $x = 0.02$ and 0.08 were taken from the most interior part of the chimney, whereas the subsample with $x = 0.17$ was taken from the middle region of the chimney wall. It should be noted that the differences in the mineral composition were due to the highly fluctuating and variable physicochemical conditions during the mineralization reactions.[25] Figure 1 shows diagrams of the crystal structure and atomic planes of chalcopyrite, which crystallizes in a tetrago-

[*] Prof. R. Ang, Dr. A. U. Khan, Dr. N. Tsujii, Prof. T. Mori
National Institute for Materials Science (NIMS)
International Center for Materials Nanoarchitechtonics (MANA)
Namiki 1-1, Tsukuba 305-0044 (Japan)
E-mail: rang@scu.edu.cn
MORI.Takao@nims.go.jp
Prof. R. Ang
Key Laboratory of Radiation Physics and Technology
Ministry of Education, Institute of Nuclear Science and Technology
Sichuan University
Chengdu 610064 (China)
Dr. K. Takai
Department of Subsurface Geobiological Analysis and Research (D-SUGAR) (Japan)
Agency for Marine-Earth Science and Technology (JAMSTEC)
Yokosuka 273-0061 (Japan)
Dr. R. Nakamura
RIKEN Center for Sustainable Resource Science
Hirosawa 2-1, Wako, Saitama 351-0198 (Japan)
E-mail: ryuhei.nakamura@riken.jp

Supporting information and ORCID(s) from the author(s) for this article are available on the WWW under http://dx.doi.org/10.1002/anie.201505517.

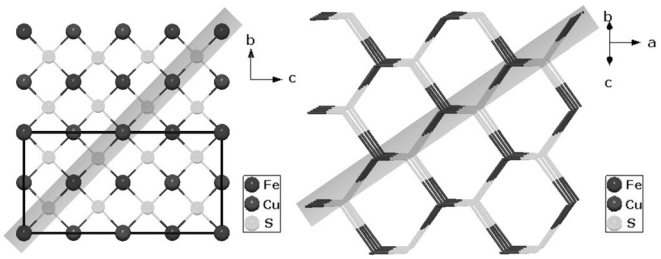

Figure 1. Crystal structure of $Cu_{1+x}Fe_{1-x}S_2$. Ball-and-stick model of the crystal structure (left) viewed along the *a*-axis with the black lines indicating the unit cell. Stick model (right) showing the characteristic honeycomb structure of chalcopyrite. The identical atomic arrangement is highlighted in gray in the two structures, but the projection is along different axes.

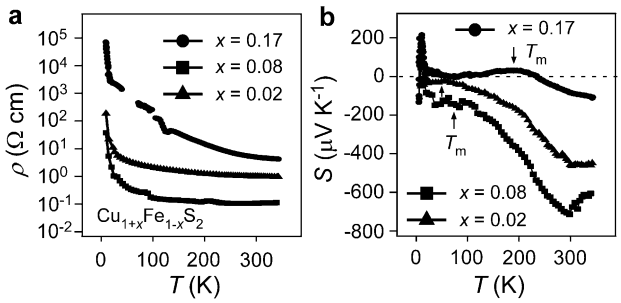

Figure 3. Formation of thermoelectricity by $Cu_{1+x}Fe_{1-x}S_2$. a) Temperature dependence of resistivity ρ in three natural samples of $Cu_{1+x}Fe_{1-x}S_2$. b) Temperature dependence of thermoelectric power *S* for the three samples.

nal lattice with a space group of $I\bar{4}2d$ and forms a characteristic honeycomb structure.[26] All the Fe and Cu atoms are surrounded by a tetrahedron of S atoms. The highlighted planes (light gray) show the zigzag pattern of the atomic arrangement, which likely contributes to phonon scattering. An X-ray diffraction (XRD) Rietveld refinement of the power pattern indicates that three natural samples have a single phase with a standard chalcopyrite structure. For $x = 0.08$, the refined lattice parameters *a* and *c* are 5.278 and 10.402 Å, respectively (see Figure S1 in the Supporting Information).

To probe the microstructures of natural $Cu_{1+x}Fe_{1-x}S_2$, we performed scanning electron microscopy (SEM; Figure 2). SEM analysis revealed that the natural chalcopyrite with $x = 0.08$ had a layered structure. The three examined natural samples were found to contain morphological diversity, which is characteristic of chalcopyrite minerals (see Figures S2 and S3 in the Supporting Information) and suggests that the different microstructures contribute to differences in the physical and chemical behaviors of these minerals. These findings indicate that the SEM analysis of natural deep-sea minerals may provide important insights into the relationship between the surface morphology and the physical and chemical functions as well as behaviors of chalcopyrite minerals.

To examine the functional properties of the natural $Cu_{1+x}Fe_{1-x}S_2$ samples, we first measured the resistivity (ρ) as a function of temperature (*T*). The three examined natural samples exhibited excellent conductive behavior with semiconductive characteristics (Figure 3a). The overall resistivity decreased as the amount of *x* decreased, because of the emergence of doped carriers. The value of ρ_{300K} for $x = 0.17$, 0.08, and 0.02 was 4.97, 0.11, and 1.01 Ω cm, respectively (see Table S1 in the Supporting Information). The increase in resistivity for the sample with $x = 0.02$ compared to the one with $x = 0.08$ is attributable to the enhancement of a random Coulomb potential resulting from the natural doping.

To further examine the evolution of electronic states in $Cu_{1+x}Fe_{1-x}S_2$, we measured the thermoelectric power (*S*) as a function of temperature *T* (Figure 3b), where the sign of *S* is altered. As *S* is an intrinsic property of the material, it is typically not affected by the microstructure. For $x = 0.17$, the sign of *S* changes from negative to positive around 235 K as *T* decreases (Figure 3b). At lower temperatures, two unusual peaks are observed: a broad peak (T_m; 32 μV K^{-1}, 186 K) and a sharper peak (T_p; 215 μV K^{-1}, 11 K), which indicates that the majority of charge carriers are of the hole type (p-type). Notably, for $x = 0.08$ and 0.02, the T_p peak completely disappears, whereas the T_m peak becomes wider and rapidly shifts to a lower temperature, at which *S* displays highly negative values, thereby demonstrating that the majority of charge carriers are of the electron type (n-type), in accordance with the negative Hall coefficient R_H (see Figure S4 in the Supporting Information). The S_{300K} term reached remarkable values of −713 and −457 μV K^{-1} for $x = 0.08$ and 0.02, respectively. This finding also infers that more electrons are activated at room temperature in minerals with a higher Fe content. For $x = 0.08$, the carrier mobility μ_{300K} and carrier density n_{300K} is 1.8 cm^2 V^{-1} s^{-1} and 3.5×10^{19} cm^{-3}, respectively, as determined from the relationships $R_H = 1/ne$ and $\mu = 1/ne\rho$. In addition to the doped carriers, the Fe magnetic moment may also be critical for producing large *S* values, thus highlighting the potential importance of the coupling between magnetic ions and doped carriers, based on the fact that synthetic $CuFeS_2$ shows an antiferromagnetic ordering at a Néel temperature of 823 K.[6]

Understanding the origin of the T_m peak and the conduction mechanism of the natural chalcopyrite samples is of critical importance for rationally designing thermoelectric materials. In terms of Mott's formula for determining the charge contribution, the character of *S* can, in general, be qualitatively described by Equation (1).

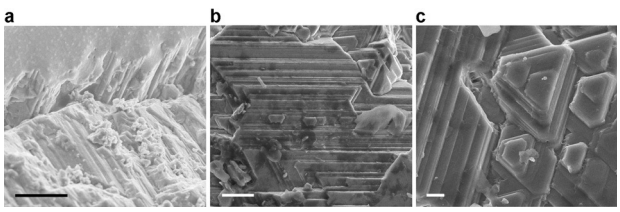

Figure 2. Surface morphology of a natural sample of $Cu_{1+x}Fe_{1-x}S_2$ ($x = 0.08$) showing the characteristic layered structure. a) Areas showing the cracked layered structure in the natural sample $Cu_{1+x}Fe_{1-x}S_2$ ($x = 0.08$), scale bar: 10 μm. b) Densely layered structure, scale bar: 5 μm. c) Triangular pattern surrounded by the layered structure, scale bar: 1 μm.

$$S = -\frac{\pi^2}{3}\frac{k_B^2 T}{e}\frac{\sigma'(E_F)}{\sigma(E_F)} \quad (1)$$

Here, k_B is the Boltzmann constant, $\sigma(E_F)$ is the conductivity at the Fermi level E_F, and σ' denotes $d[\sigma(E)]/dE$.[27] If one assumes σ' is a constant that is accompanied by isotropic electrical transport properties, namely, $\sigma^{-1}=\rho$, then $\Delta S/S_0 \propto \Delta\rho/\rho_0$ can be derived. A plot of $\Delta S/S_0$ versus $\Delta\rho/\rho_0$ for $x=0.17$ over a range of temperatures (Figure 4) shows that all of the experimental data in the vicinity of the T_m peak at T_0 from 155 to 300 K deviate from the above theoretical prediction regarding the linearity between thermoelectric power $S(T)$ and resistivity $\rho(T)$. These results signify that the mechanism controlling $S(T)$ in the natural sample is unique compared to conventional thermoelectric materials.[28]

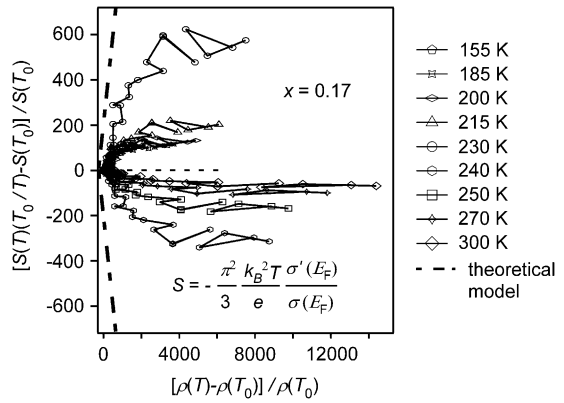

Figure 4. Correlation between thermoelectric power $S(T)$ and resistivity $\rho(T)$. Relative changes of $\Delta S/S_0$ versus $\Delta\rho/\rho_0$ in the natural sample with $x=0.17$ at various temperatures ($T_0=155$, 185, 200, 215, 230, 240, 250, 270, and 300 K). The experimental data substantially deviate from the linear relationship predicted by Mott's formula, which is indicated by the dotted line.

To better discern the intrinsic transport mechanism of $Cu_{1+x}Fe_{1-x}S_2$, we analyzed the temperature dependence of S on the basis of spin–wave theory. For $x=0.08$ and 0.02, the field-cooling (FC) magnetization $M(T)$ and $M(H)$ loop hysteresis demonstrate that an anomaly exists at low temperatures, that is, the weak localized ferromagnetic interaction arising from the additional Fe moments (see Figure S5 in the Supporting Information). Even so, the strong high-temperature antiferromagnetic phase dominates the magnetic properties for three natural samples. In principle, for (anti)ferromagnetic materials, electrons can be scattered by spin waves, which produces a magnon drag effect.[3] To examine this phenomenon, we developed the theory of magnon drag to simulate the experimental data by using Equation (2).

$$S = S_0 + S_{3/2}T^{3/2} + S_4T^4 \quad (2)$$

Here, S_0 is the value of S at $T=0$, the $S_{3/2}T^{3/2}$ term stems from electron–magnon scattering, and the S_4T^4 term is related to spin–wave fluctuation in the antiferromagnetic phase. Using

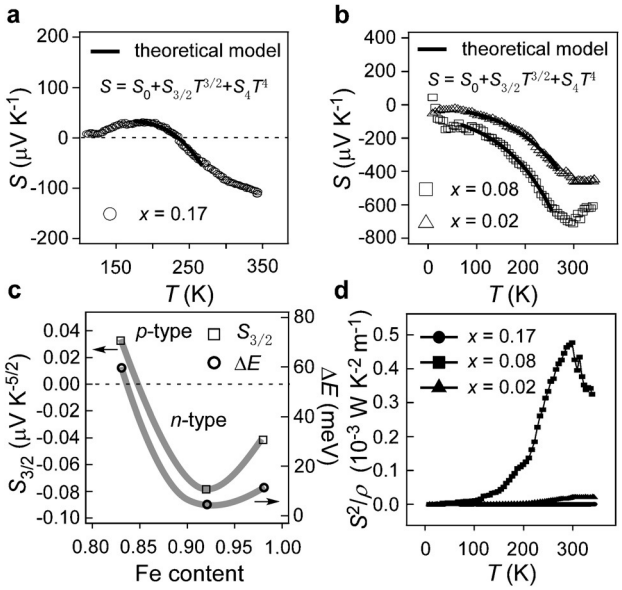

Figure 5. a,b) Temperature dependence of S for $Cu_{1+x}Fe_{1-x}S_2$ samples with $x=0.17$ (a) and $x=0.08$ and 0.02 (b). The symbols represent experimental data and the solid lines correspond to the theoretical simulation based on the model of magnon drag, $S=S_0+S_{3/2}T^{3/2}+S_4T^4$. c) The obtained parameters $S_{3/2}$ and ΔE are plotted as a function of Fe content, where $S_{3/2}$ represents the electron–magnon scattering process and ΔE is the activation energy. d) Temperature dependence of the power factor, S^2/ρ, for the three samples.

this model of magnon drag, the predicted values for the three samples closely matched the $S(T)$ data (Figure 5a,b). As the absolute value of $S_{3/2}$ is nearly six orders of magnitude larger than that of S_4 (see Table S2 in the Supporting Information), the electron–magnon scattering dominates the $S(T)$ curve. Thus, the T_m peak is predicted to originate from the magnon drag arising from the strong electron–magnon interaction.

To gain further insight into the correlation between the magnon drag, doped carriers, and S, we plotted the parameters S_0, $S_{3/2}$, and S_4 as a function of x (see Table S2 in the Supporting Information). The absolute values of S_0, $S_{3/2}$, and S_4 for $x=0.08$ were the largest among the examined samples, and are consistent with the large S, small ρ, and high power factor values that were observed for the $x=0.08$ sample. In contrast to S_0 and S_4, the dependence of $S_{3/2}$ on Fe content is a novel finding (Figure 5c). The sign of $S_{3/2}$ changes from positive to negative with an increase in Fe content, thus indicating that the electronic state has been altered from hole (p-type) to electron (n-type) charge carriers, and suggesting that the orbital degree of freedom of the Fe 3d band plays a critical role in the charge dynamics of antiferromagnetic orbital ordering. In addition, because the magnon drag forms in the low x region, the electron–magnon scattering presides over the $S(T)$ property, thus indicating that the doped carriers and antiferromagnetic spins are strongly coupled. Furthermore, from the viewpoint of electrical transport, the $\rho(T)$ data are consistent with the thermally activated conduction model shown in Equation (3) (see Figure S6 in the Supporting Information).

$$\rho(T) = \rho_0 \exp(\Delta E/k_B T) \quad (3)$$

Here ΔE is the activation energy.[27] Notably, the fitted energy gap of ΔE (60.1, 4.9, and 11.8 meV for $x = 0.17$, 0.08, and 0.02, respectively), which verifies the existence of localized Fe spins, is markedly smaller than that of artificial chalcopyrite.[12,20–22] It is noted that the experimental $S(T)$ result is well-described by the electron–magnon scattering up to about 200 K, while it deviates from the theoretical lines at higher temperatures. In particular, the power factor S^2/ρ shows an abrupt enhancement above 200 K for $x = 0.08$ (Figure 5 d), in agreement with that of R_H and n (see Figure S4 in the Supporting Information). It should be emphasized that the large effective mass (m^*) produces the high power factor and large S value above 200 K, since low μ and high n values are responsible for high m^* values. At room temperature, the sample with $x = 0.08$ displays the largest m^* value, reaching $1.6\,m_0$, where m_0 is the electron mass. Based on these results, we can conclude that the unexpected generation of thermoelectricity by natural chalcopyrite, which is characterized by a large S value and a high power factor, is driven by the robust electron–magnon scattering and the large m^* value.

In terms of the thermal conductivity κ, the phononic component κ_{ph} dominates for the three natural samples because of the negligible electronic component κ_e (see Figure S7 in the Supporting Information). Overall, the value of κ_{300K} (3.1, 4.8, and 2.2 $W K^{-1} m^{-1}$ for $x = 0.17$, 0.08, and 0.02) is low due to the effective phonon scattering. Finally, the thermoelectric performance is evaluated by the dimensionless figure of merit $ZT = S^2 T/\rho\kappa$. For the optimal sample with $x =$ 0.08, the value of ZT can reach 0.03 at room temperature (see Figure S7 in the Supporting Information), thus indicating that the natural chalcopyrite semiconductor could be considered as a promising thermoelectric energy material. It is quite remarkable that the spontaneous doping process during the precipitation of deep-sea hydrothermal vent minerals resulted in the natural enhancement of thermoelectric properties, which seems to be reminiscent of high-performance thermoelectricity based on natural mineral tetrahedrites.[29]

We have demonstrated the direct generation of thermoelectricity by natural chalcopyrite, $Cu_{1+x}Fe_{1-x}S_2$, which was shown to have a large S value and a high power factor in the low x region, in which electron–magnon scattering and large m^* values were detected. As the doped carriers within $Cu_{1+x}Fe_{1-x}S_2$ exhibit strong coupling with localized spins, the atypical alternation between p- and n-type carriers may be important for modulating the charge dynamics characterized by 3d orbital degrees of freedom. As these novel thermoelectric properties were only found in natural, but not synthetic, chalcopyrite, it may be technically feasible to design surface-morphology-engineered devices using naturally abundant materials for producing low-cost thermoelectricity or electron/hole carriers.

Experimental Section

Several samples of natural chalcopyrite minerals ($Cu_{1+x}Fe_{1-x}S_2$) were obtained from a hydrothermal vent site named Snow Chimney (SC; 22°10.825′S, 176°36.095′W, 1908m), which is located in the Mariner field of the Lau Basin, using the deep-sea submersible vehicle Shinkai 6500.[23] For microstructural characterization, we utilized field-emission-scanning electron microscopy (FE-SEM, Hitachi S-4800) operated at 10 kV with a working distance of 10 mm. The average stoichiometry and composition of the measured samples was determined by energy-dispersive X-ray spectroscopy (EDX, EMAX ENERGY; from Horiba, Ltd.), which was attached to the scanning electron microscope and operated at 15 kV and a working distance of 15 mm. The natural samples were treated by grinding, polishing, or coating to avoid the introduction of any artifacts. For the characterization, the cracked surfaces of different samples collected from various areas at the vent site were examined. Crystal structure analysis was performed by XRD using the Philips X'pert PRO diffractometer with Cu $K\alpha$ radiation. The structural refinement was based on the Rietveld analysis.

The thermoelectric properties of the $Cu_{1+x}Fe_{1-x}S_2$ samples were measured based on electrical and thermal transport using a standard four-probe configuration in a physical property measurement system (PPMS, Quantum Design). The measurements of the temperature dependence of resistivity $\rho(T)$, thermoelectric power $S(T)$, and thermal conductivity $\kappa(T)$ were performed over a wide temperature range from 5 to 340 K under vacuum. The Hall coefficient R_H and carrier density n were determined by Hall measurement using a standard five-probe method and conducted by PPMS. Measurement of the magnetic properties was performed in a Quantum Design superconducting quantum interference device (SQUID) system.

Acknowledgements

We are grateful to Prof. Kazuhito Hashimoto for inspiring this work. This work was financially supported by the NIMS Open Innovation Center (NOIC) of Japan. R.A. thanks the Sichuan University talent introduction research funding (grant no. 1082204112044) and Sichuan University outstanding young scholars research funding (grant no. 2015SCU04A20) of China for financial support.

Keywords: energy conversion · materials science · semiconductors · solid-state chemistry · thermoelectric materials

How to cite: *Angew. Chem. Int. Ed.* **2015**, *54*, 12909–12913
Angew. Chem. **2015**, *127*, 13101–13105

[1] J. R. Sootsman, D. Y. Chung, M. G. Kanatzidis, *Angew. Chem. Int. Ed.* **2009**, *48*, 8616–8639; *Angew. Chem.* **2009**, *121*, 8768–8792.
[2] Y. L. Chen, Z. K. Liu, J. G. Analytis, J.-H. Chu, H. J. Zhang, B. H. Yan, S.-K. Mo, R. G. Moore, D. H. Lu, I. R. Fisher, S. C. Zhang, Z. Hussain, Z.-X. Shen, *Phys. Rev. Lett.* **2010**, *105*, 266401.
[3] K. Koumoto, T. Mori, *Springer Ser. Mater. Sci.* **2013**, *182*, 1–387.
[4] P. I. Ekwo, C. E. Okeke, *Energy Convers. Manage.* **1992**, *33*, 159–164.
[5] G. Donnay, L. M. Corliss, J. D. H. Donnay, N. Elliott, J. M. Hastings, *Phys. Rev.* **1958**, *112*, 1917–1923.
[6] T. Teranishi, *J. Phys. Soc. Jpn.* **1961**, *16*, 1881–1887.
[7] J. A. Tossell, D. S. Urch, D. J. Vaughan, G. Wiech, *J. Chem. Phys.* **1982**, *77*, 77–82.
[8] M. Fujisawa, S. Suga, T. Mizokawa, A. Fujimori, K. Sato, *Phys. Rev. B* **1994**, *49*, 7155–7164.
[9] R. Nakamura, T. Takashima, S. Kato, K. Takai, M. Yamamoto, K. Hashimoto, *Angew. Chem. Int. Ed.* **2010**, *49*, 7692–7694; *Angew. Chem.* **2010**, *122*, 7858–7860.

[10] S. W. Lovesey, K. S. Knight, C. Detlefs, S. W. Huang, V. Scagnoli, U. Staub, *J. Phys. Condens. Matter* **2012**, *24*, 216001.
[11] I. S. Lyubutin, C.-R. Lin, S. S. Starchikov, Y.-J. Siao, M. O. Shaikh, K. O. Funtov, S.-C. Wang, *Acta Mater.* **2013**, *61*, 3956 – 3962.
[12] N. Tsujii, T. Mori, *Appl. Phys. Express* **2013**, *6*, 043001.
[13] C. H. L. Goodman, R. W. Douglas, *Physica* **1954**, *20*, 1107 – 1109.
[14] I. G. Austin, C. H. L. Goodman, A. E. Pengelly, *J. Electrochem. Soc.* **1956**, *103*, 609 – 610.
[15] K. G. Nikiforov, *Prog. Cryst. Growth Charact. Mater.* **1999**, *39*, 1 – 104.
[16] W. H. Koschel, F. Sorger, J. Baars, *J. Phys.* **1975**, *36*, C3:177 – 181.
[17] W. H. Koschel, M. Bettini, *Phys. Status Solidi B* **1975**, *72*, 729 – 737.
[18] K. Sato, Y. Harada, M. Taguchi, S. Shin, A. Fujimori, *Phys. Status Solidi A* **2009**, *206*, 1096 – 1100.
[19] J. C. Woolley, A.-M. Lamarche, G. Lamarche, M. Quintero, I. P. Swainson, T. M. Holden, *J. Magn. Magn. Mater.* **1996**, *162*, 347 – 354.
[20] I. G. Austin, C. H. L. Goodman, A. E. Pengelly, *Nature* **1956**, *178*, 433.
[21] T. Hamajima, T. Kambara, K. I. Gondaira, T. Oguchi, *Phys. Rev. B* **1981**, *24*, 3349 – 3353.
[22] T. Teranishi, K. Sato, K. Kondo, *J. Phys. Soc. Jpn.* **1974**, *36*, 1618 – 1624.
[23] N. Tsujii, T. Mori, Y. Isoda, *J. Electron. Mater.* **2014**, *43*, 2371 – 2375.
[24] K. Takai, T. Nunoura, J. Ishibashi, J. Lupton, R. Suzuki, H. Hamasaki, Y. Ueno, S. Kawagucci, T. Gamo, Y. Suzuki, H. Hirayama, K. Horikoshi, *J. Geophys. Res.* **2008**, *113*, G02031.
[25] M. K. Tivey, *Geochim. Cosmochim. Acta* **1995**, *59*, 1933 – 1949.
[26] C. H. L. Goodman, *Nature* **1957**, *179*, 828 – 829.
[27] N. F. Mott, E. A. Davis, *Electronic processes in non-crystalline material*, Clarendon, Oxford, **1971**.
[28] A. Asamitsu, Y. Moritomo, Y. Tokura, *Phys. Rev. B* **1996**, *53*, R2952 – 2955.
[29] X. Lu, D. T. Morelli, Y. Xia, F. Zhou, V. Ozolins, H. Chi, X. Y. Zhou, C. Uher, *Adv. Energy Mater.* **2013**, *3*, 342 – 348.

Received: June 15, 2015
Published online: September 2, 2015

